Journal of Drug Delivery Science and Technology 53 (2019) 101167

Contents lists available at ScienceDirect

Journal of Drug Delivery Science and Technology

journal homepage: www.elsevier.com/locate/jddst

Characterization of jets for impulsively-started needle-free jet injectors: Influence of fluid properties

Pankaj Rohilla[a], Yatish S. Rane[a], Idera Lawal[a], Andrew Le Blanc[a], Justin Davis[a], James B. Thomas[a], Cormak Weeks[a], Whitney Tran[b], Paul Fisher[c], Kate E. Broderick[c], Jonathan A. Simmons[a,d], Jeremy O. Marston[a,*]

[a] Department of Chemical Engineering, Texas Tech University, Lubbock, TX, 79409, USA
[b] Department of Mathematics & Statistics, Texas Tech University, Lubbock, TX, 79409, USA
[c] Inovio Pharmaceuticals, 10480 Wateridge Circle, San Diego, CA, 92121, USA
[d] Department of Mechanical Engineering, Texas Tech University, Lubbock, TX, 79409, USA

ARTICLE INFO

Keywords:
Needle-free injection
Liquid jet
Impact force
Rheology

ABSTRACT

An experimental study was performed to assess the hydrodynamics of liquid jets used for needle-free injection, where the typical orifice diameter is ~155 μm and velocity is in range of ~ 60–140 m/s. The jet is impulsively started by a spring-piston that forces a plunger through a cartridge filled with the liquid. Liquid exiting the orifice then forms a jet. However, despite a fixed spring force, the jet speed can vary significantly depending on the fluid physical properties - in particular - the effective viscosity. Since in practice a wide range of fluids may be used for injection, we seek herein to study the jet formation and speed for a broad range of fluids, characterized by viscosity or rheological profile. In addition, we also characterize the jet performance with a peak impact force, measured by a dynamic load cell, and ex-vivo injection experiments on porcine tissue. We find that jet speeds and impact forces decrease in a non-linear fashion with increasing viscosity, but that shear-thinning effects are significant and can render high jet speeds (> 100 m/s) even for low-shear viscosities μ_0~100 Pa.s.

1. Introduction

Routine administration of vaccines via hypodermic syringes is known to cause mild to severe anxiety in patients with needle-phobia (trypanphobia), and affects approximately one in ten patients in the US [1,2]. More grave, however, are needle-stick injuries for health professionals and patient cross-contamination due to needle re-use in developing nations [3,4]. The 2002 World Health Report [5] from the World Health Organization (WHO) indicated that 2 million health-care workers are subject to needle-stick injuries each year, which causes nearly 40% of all cases of Hepatitis B and C in health-care workers, whilst the financial cost of treating needle-stick injury is estimated at up to $3,000 per incident [6,7]. The Safe Injection Global Network (SIGN) and Global Vaccine Action Plan (GVAP) of the WHO have therefore recommended supporting the development of needle-free injection technologies [8,9], noting that they reduce the risk of spreading infection.

Needle-free injection is a form of drug delivery through the skin without the use of hypodermic needles and syringes. There are different forms of needle-free injection [10,11], such as micro-needle patches specifically for intradermal (ID) delivery, powder-based ballistic delivery and jet injectors, which rely on a high-speed jet to puncture the skin. The predominant use of needle-free jet injectors in the past has been for subcutaneous (SC) and intramuscular (IM) delivery [11–14], but are now being explored for intradermal (ID) delivery, as documented in recent clinical trials [15–20].

The basic operating premise of jet injection is that a high upstream pressure, typically created using either a spring or compressed gas mechanism, forces a jet at high-speed, $V_{jet} \sim \mathcal{O}(100 m/s)$, from a narrow orifice, $D_0 \sim \mathcal{O}(100 \mu m)$. Studies with both commercial and custom devices in the literature have primarily been in-vitro [21–27] or ex-vivo [28–34] and typically consider large doses in the milliliter range, but some novel approaches including piezoelectrics [35], lasers [36–39] and explosives [40] are now also exploring delivery in the nanoliter range. While most of these studies have focused on low-viscosity fluids, the injectable drug market includes concentrated solutions with potentially high viscosities ($\mu \gtrsim 200$ mPa.s) [41,42], indicating the need to address the influence of fluid viscosity. In addition, the advent of novel

* Corresponding author.
E-mail address: jeremy.marston@ttu.edu (J.O. Marston).

https://doi.org/10.1016/j.jddst.2019.101167
Received 8 May 2019; Received in revised form 27 June 2019; Accepted 18 July 2019
Available online 25 July 2019
1773-2247/

nucleic acid vaccines [43–45] necessitates an assessment of the effect of rheological profile on injection. With regards to hydrodynamic considerations, refs [46,47] are of particular relevance; A mechanical force balance was derived in Ref. [46], accounting for viscous losses through a discharge coefficient. This model compared favorably to experimental data for the piston displacement, however, non-Newtonian solutions were not explicitly considered. In addition, the recent study of [47] reports on CFD simulations of flow in the orifice region, which again gave good agreement with experimental data for jet speeds. This latter paper also addresses the issue of viscosity reduction due to heating caused by the high shear rates in the orifice region, which has important implications for non-Newtonian fluids as well.

In this paper, we focus specifically on the effect of fluid viscosity and rheological properties for impulsively-started jets using a spring mechanism. We use a single device and orifice size paired with different spring constants to study the influence of fluid properties, and characterize the jet performance with (i) jet speed, (ii) impact force, and (iii) delivery efficiency in ex-vivo tissues. In light of the observations of [47], a key factor in our analysis is the nature of the fluid, i.e. Newtonian vs. non-Newtonian.

2. Materials and methods

2.1. Injection device

For this study we used the Bioject ID Pen, which is a streamlined spring-powered jet injector device originally designed for injection of 0.1 mL. The device, shown in Fig. 1(a) is comprised of a spring housed in an upper chamber which is cocked by manually extending the arm on the outside of the chamber. A cartridge, shown in Fig. 1(b), pre-loaded with fluid is then inserted into the front end of the device and locked in place by rotation. The injection is then triggered manually by pressing on an external trigger ring, whereupon the spring is released and a piston hits the rear end of the plunger. After injection, the used cartridge is released from by pulling on a release ring. By modification of the spring constant and/or piston stroke length, both the spring force and expelled volume can be varied. Here, we examined three different configurations - (i) spring force 63 lbs/in with V = 100 μL (ID Pen 61), (ii) spring force 55 lbs/in with V = 100 μL (ID Pen 55), and (iii) spring force 63 lbs/in and V = 50 μL (ID Pen 46).

The upper cartridge inner diameter where the plunger travels is D_p = 4.57 mm, whilst the orifice diameter is $D_o \approx 157$ μm. The contraction from the plunger to the orifice is a multi-tier taper with the main taper section having a cone angle of approximately 5°. In practice, a stand-off distance S between the orifice and the skin surface can be implemented by use of a spacer ring, shown in Fig. 1(b) and (c), fitted to the end of the cartridge.

2.2. Materials used and their properties

A range of fluids were considered in this study to vary both viscosity and rheological profile. For Newtonian fluids, we used water (ultrapure milliQ) and glycerol (Macron) solutions with the percentage of glycerol in water ($\%_{w/w}$) varying from 0 to 100%. Since many novel therapeutics (e.g. macromolecular proteins and nucleic acids) in suspension form are shear-thinning in nature, our focus for non-newtonian fluids was on shear-thinning behavior. Sodium carboxymethyl cellulose (CMC) (average molecular weight $\sim 7 \times 10^5$, degree of substitution = 0.8–0.95, Sigma Aldrich) solutions were prepared as model non-newtonian fluids in concentrations ranging from 0.125 $\%_{w/w}$ to 2 $\%_{w/w}$ in water. The choice of CMC was governed by widespread commercial availability and extensive characterization in the literature [48,49]. Rheological characterization was performed using a cone-and-plate geometry (25 mm diameter and 1.992° angle) on a DHR-2 rheometer (TA Instruments) at a temperature of 21 ± 1 °C. The sample was conditioned for 10 min (Temperature soak: 7 min, Equilibration: 3 min) after loading. A modified bottom plate was used as a solvent trap with Silicon oil as the solvent. The flow behavior of the CMC solutions was measured using a flow ramp with a shear rate range of 0.01–1000 s^{-1} for 2 min as test time. For non-Newtonian fluids, the rheological data were best fitted by the Cross model, given by

$$\frac{\mu_a - \mu_\infty}{\mu_0 - \mu_\infty} = \frac{1}{1 + (\lambda\dot{\gamma})^n} \quad (1)$$

where μ_a is the apparent viscosity for a given shear rate, $\dot{\gamma}$, μ_0 and μ_∞ are the asymptotic plateaus at zero and infinite shear rates, and λ and n are the time constant and rate index respectively. For practical purposes, the reciprocal of the time consant, $1/\lambda$, provides an estimate of the critical shear rate at which shear-thinning effects dominate and the fluid behaves as a power-law fluid. Example rheological data is shown in Fig. 2 for various concentrations. Shear rates in the upstream cartridge region and the orifice can be estimated as $\dot{\gamma} \sim 2V_p/D_p$ and $2V_j/D_j$, respectively. This gives us a range of effective shear rates of $\mathcal{O}(10^2 - 10^6)$ s^{-1}, so we focus on fitting to the data above $\dot{\gamma} = 10^0$ s^{-1}.

The summary of fluids used, and the corresponding viscosities and rheological parameters are shown in Table 1 (Newtonian) and 2 (non-Newtonian).

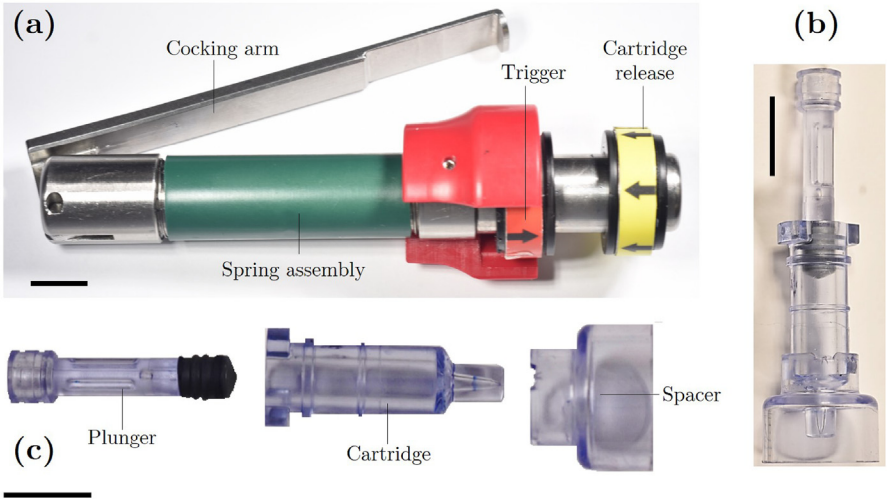

Fig. 1. (a) ID Pen device (b) standard cartridge (0.1 ml) with 2 mm spacer, and (c) plunger, cartridge and spacer. Scale bar: 1 cm.

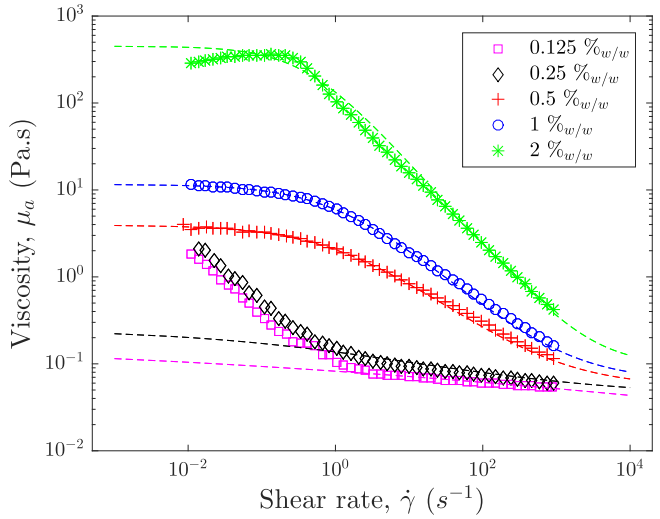

Fig. 2. Rheological data plotted as viscosity versus shear rate. The dashed lines through the data points represent fits to the data with the Cross model, given in equation (1). [See Table 2 for fit parameters].

2.3. Imaging

In order to derive both the jet speeds and early-time jet dynamics, we employed high-speed video cameras (Phantom V711 and V1611) from Vision Research Ltd. A single side-view perspective was used to measure the plunger displacement, which is used to calculate the instantaneous plunger velocity, from which we can derive the flow rate and instantaneous exit (jet) speed. The camera was operated at a frame rate of 30,000 fps. In addition, using a Nikon micro-nikkor 60 mm lens, we achieved typical effective pixel sizes of between 20 and 40 μm/px.

A sequence of typical images used for tracking the plunger is shown in Fig. 3(a). In brief, we mark four outer points in the first video frame and employ image analysis either using commercial tracking software (Photron Fastcam Analysis) or custom-written routine in Matlab to track these four points frame-by-frame. The fifth (internal) tracking point is the plunger tip (see Fig. 3(b)), and the plunger displacement is then calculated as an average relative to the four external points. Using the four external points, we can ensure a true vertical displacement through the cartridge is calculated since any vibrations caused by recoil are taken into account.

2.4. Impact force measurement

A miniature load button cell (Futek - LLB 130, 50 lb, Item # FSH03880) was placed beneath the orifice opening of the nozzle of the bioject device so that the liquid jet impinges on to the center of button cell. The force measurements were made at a rate of 4,800 samples per second. The load cell mechanism of the force measurement was based on a metal foil strain gauge. A standoff distance of 2 mm was used to allow for small vertical motion of the device in operation.

2.5. Ex-vivo injections

For demonstration of the jet injection, we performed a limited number of trials into porcine tissue procured from a local butcher. The samples were cut into approximately 2-inch sections and injected with 100 μL of fluid (DI water, 80% glycerol or 0.5% CMC). To aid with visualization, each fluid was supplemented with Trypan blue dye (approximate concentration of 1 mg/mL). The samples were medially sectioned across the injection site and photographed with a Nikon DSLR camera. The injection depth and overall dispersion pattern were measured.

Table 2
Cross model constants from rheological data of the CMC solutions.

CMC (%)*w/w*	μ_0 (Pa.s)	μ_∞ (Pa.s)	λ (s)	*n*
0.125	0.181	0.001	6	0.107
0.25	0.214	0.042	1.86	0.291
0.5	3.948	0.055	0.92	0.633
1	11.59	0.065	0.94	0.722
2	450	0.095	2.5	0.95

3. Results and discussion

3.1. Jet start-up observations

The total jetting time depends upon both the volume expelled and fluid viscosity, but typically lasts between 20 and 80 ms. Of this, the first 2–3 ms is herein referred to as the 'start-up' phase during which the impulsive action of the spring-piston causes a rapid pressure rise in the liquid inside the cartridge, and an interplay between compression of the plunger tip and unsteady fluid motion through the orifice. After this, the plunger achieves an approximately linear motion, which is considered the 'steady-stream' phase.

During the start-up phase, we observe that the initial exit of fluid is dominated by the high-velocity associated with the pressure impulse; Examples of this are shown in Fig. 4 for different fluids, which are typical for the range of fluids used in this study. In each sequence the true pressure spike ($\mathcal{O}(10^7)$ Pa) occurs approximately in the third or fourth image, whilst the fluid ejected prior to this is an artefact of the triggering mechanism. As such, an extremely small volume of fluid is ejected prior to the main high-velocity jet. When the high-velocity fluid interacts with the pre-jet fluid, atomization occurs which results in a localized spray of micron-sized droplets. It is observed, however, that this atomization is extremely short-lived and does not contribute to any significant fluid loss. Thus, the main steady-stream jet, as depicted by the final image in each sequence, is established very rapidly after the pressure impulse, within approximately 3 ms.

Corresponding image sequences for CMC jets are presented in Fig. 5 for both 0.25% and 1% concentrations (μ_0 = 0.214 and 11.59 Pa.s, respectively). In these startup events, we find that the atomization feature observed for water and weak glycerol solutions is absent, instead producing an elongated, thicker jet tip. However, the ultimate result is the production of a steady jet flow within several milliseconds.

A close-up image of the steady-stream phase for 80% glycerol (μ = 84 mPa.s) is presented in Fig. 6(a), which shows a coherent, slender jet (i.e. laminar regime). Based upon the calculated jet speed (see below for details), $V_j \approx 115$ m/s, the jet Reynolds number in this case is $Re_j = \rho D_j V_j/\mu \approx 260$, for which one would expect a laminar jet. For water (μ = 1 mPa.s), however, this is not the case since $Re_j \sim 2 \times 10^4$

Table 1
Physical properties of the liquids used in the experiments, where μ is dynamic viscosity and ρ is density. The glycerol solutions ($\%_G$) are presented as concentration in terms of $\%w/w$ in water.

Liquid	Water	50 $\%_G$	60 $\%_G$	70 $\%_G$	80 $\%_G$	90 $\%_G$	95 $\%_G$	100 $\%_G$
μ (Pa.s)	0.001	0.0069	0.0137	0.0296	0.084	0.215	0.482	1.31
ρ (kg/m^3)	996	1130	1156	1182	1209	1235	1248	1261

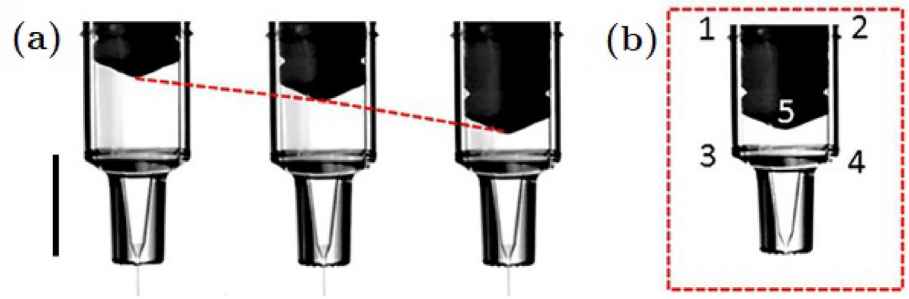

Fig. 3. (a) Typical images of the cartridge and plunger used for tracking and derivation of plunger and jet speeds. (b) The outlined image indicates the four external corner points and the internal plunger tip. *Scale bar:* 8 mm.

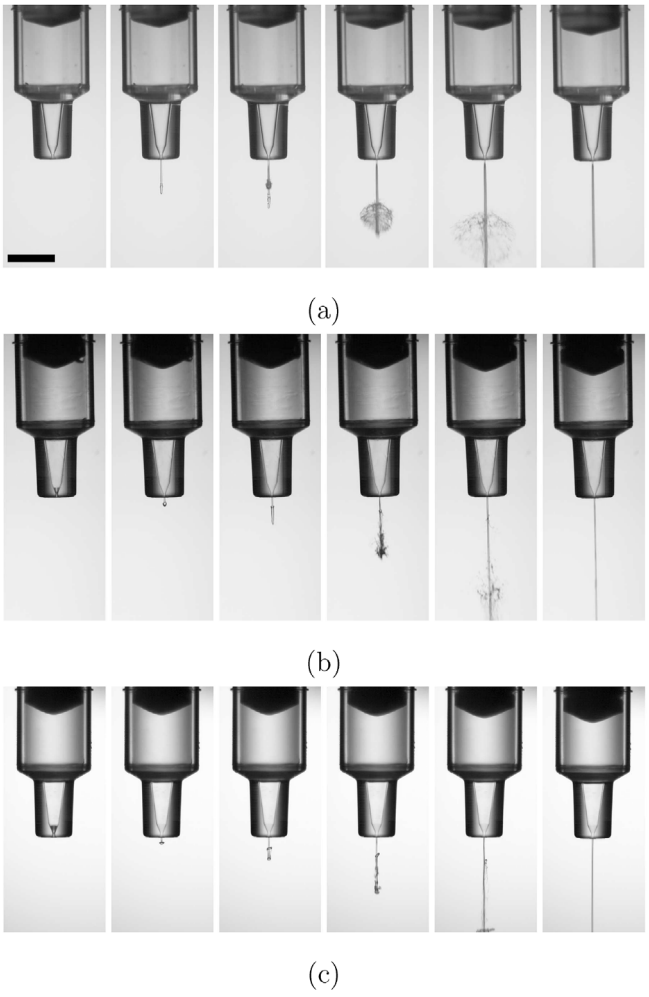

Fig. 4. Image sequences of the jet start-up phase for (a) water, (b) 50% glycerol, and (c) 80% glycerol. The scale bar in (a) is 5 mm long and the times relative to the first observed motion are (a) $t = -0.736, 0.648, 0.824, 0.894, 0.946, 2.48$ ms, (b) $t = -3.35, 3.4, 3.55, 3.7, 3.85, 6.2$ ms, (c) $t = -2.55, 2.6, 2.75, 2.9, 3.05, 6.35$ ms.

and we can observe the hallmarks of a turbulent jet stream, as shown in Fig. 6(b), which is visually characterized by a dispersed and hazy jet appearance just downstream of the orifice.

3.2. Displacement curves and jet time derivation

Example plunger displacement curves are shown in Fig. 7 for a variety of glycerol concentrations from 0 to 100%$_{w/w}$, covering a viscosity range of 0.001–1.31 Pa.s. All curves have been overlayed with

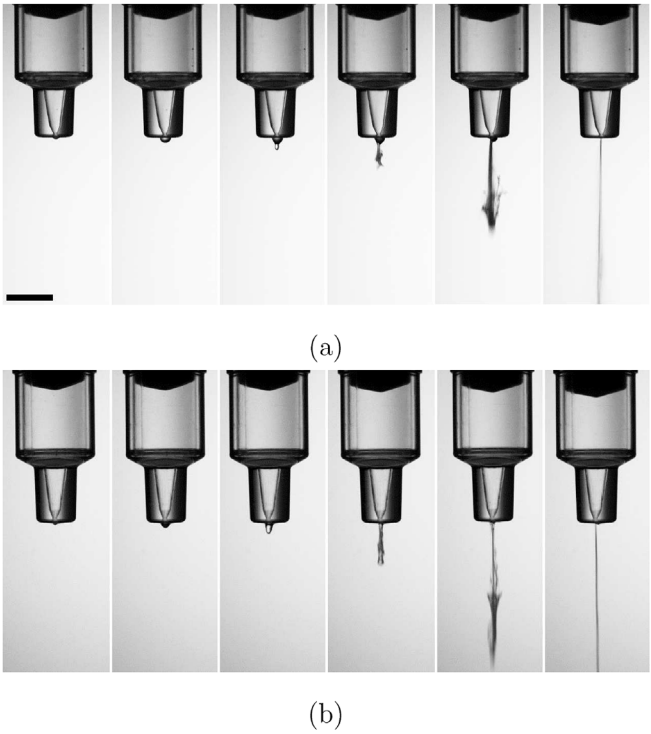

Fig. 5. Image sequences of the jet start-up phase for (a) 0.25% CMC, and (b) 2% CMC. The scale bar in (a) is 5 mm long and the times relative to the first observed motion are (a) $t = 0,7.2, 11.3, 11.53, 11.77, 13.93$ ms, (b) $t = 0,7.87, 9.13, 9.37, 9.53, 12.63$ ms.

$t = 0$ indicating the onset of the pressure impulse. The dashed box highlights the early-time region, which is shown in more detail in the inset figure for $t < 6$ ms. We observe that for $t \lesssim 1$ ms, the curves are virtually indistinguishable; In this phase, the plunger moves rapidly and attains a maximum velocity $V_p^* \approx 0.8$ m/s, which corresponds to the atomization observed in Fig. 4. Note that this maximum plunger speed is considerably higher than the steady-stream phase for $t \gtrsim 3$ ms, and it may be within this phase where the jet strikes and punctures the skin, however, we can expect a higher degree of system compliance in this transient stage [28], therefore indicating that a more detailed investigation of the impact force and impact pressure of the jet is needed.

The total duration of the jetting process is taken from the moment fluid motion is first detected until the jetting is completely arrested. In previous studies, e.g. Ref. [34], this total jetting time has been used to calculated flow rates through the orifice and thus the average jet speed. However, this can be a misleading representation of the true jet speed, as a simple visual inspection of the displacement curves easily shows. Therefore, it is more descriptive to break down the total jetting time into the discrete stages - namely - (i) the rapid pressure rise due to

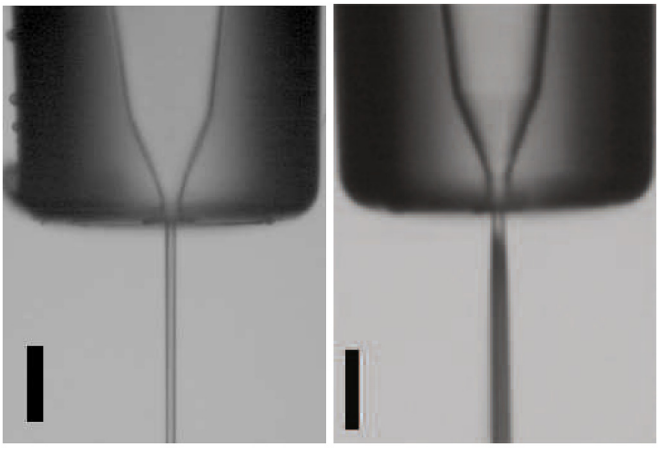

Fig. 6. Close-up images showing both (a) laminar (μ = 84 mPa.s) and (b) turbulent (μ = 1 mPa.s) steady jet streams. The scale bars are both 1 mm long.

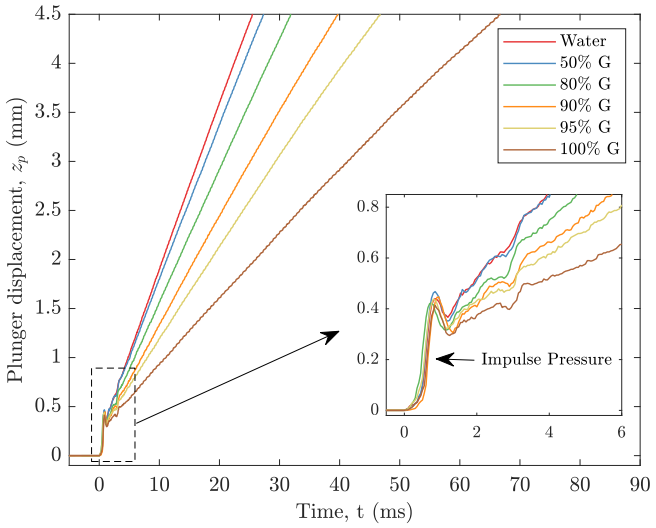

Fig. 7. Plunger tip displacement curves resulting from high-speed video tracking for various concentrations of glycerol. The plot shows the overview for times up to 25–70 ms, whilst the inset plot shows the early-time data from the dashed box for times up to 6 ms, highlighting the pressure impulse for $t \lesssim 1$ ms.

impulse of the piston ($t \lesssim 1$ ms), (ii) ringing phase caused by recoil ($t \approx 1-3$ ms), (iii) steady jet stream ($t \gtrsim 3$ ms), and (iv) deceleration as the plunger tip meets the end of the main cartridge barrel ($t \approx 30-80$ ms). The steady jet stream thus lasts for approximately 27–77 ms, which depends on the fluid viscosity, and it is in this stage where we calculate the linear slope of the $z_p - t$ curves in order to derive the plunger speed, $V_p = dz_p/dt$.

3.3. Jet speeds

The jet speed during the steady jet stream phase is derived from mass conservation, assuming incompressibility as

$$V_j = V_P\left(\frac{D_P}{D_j}\right)^2. \tag{2}$$

Note that this does not infer any information regarding the discharge coefficient or pressure loss in the taper region; this detailed fluid mechanical discussion of the flow in the cartridge and orifice region will be dealt with in a subsequent publication. The jet speeds for both the Newtonian solutions of glycerol and non-Newtonian solutions of CMC are plotted as a function of viscosity in Fig. 8(a) and (b), respectively. Focusing first on the Newtonian fluids, across the full range of viscosities ($\mu \sim \mathcal{O}(10^{-3} - 10^{0})$ Pa.s), we observe a monotonic decrease in jet speed from $V_j \approx 130$ m/s for water down to ≈ 70 m/s for pure glycerol (standard configuration shown by blue data points), with the sharpest decrease being for the high-viscosity range. With regards to the configuration of the device, we find that the reduced spring force (black data points) result in lower jet speeds, as expected where the percentage reduction of 10–12% is similar to that of the spring force (55/63). In addition, the reduced volume configuration (red data points) resulted in higher jet speeds for $\mu \lesssim 0.1$ Pa.s, but did not exhibit any notable difference for higher viscosities.

Overall, any single empirical equation fails to adequately describe the Newtonian jet speed data across the full range of viscosities, and the best simple description is a power-law model $V_j = \alpha\mu^{-\beta}$, where the data is partitioned at $\mu = 0.1$ Pa.s. For example, the standard configuration (blue data points in Fig. 8(a)) can be described by the numerical prefactor $\alpha = 103$ and the exponent $\beta = -0.04$ for $\mu \leq 0.01$ Pa.s, and $\alpha = 79$ and $\beta = -0.1443$ for $\mu \geq 0.1$ Pa.s.

The jet speeds for the non-Newtonian solutions are presented in Fig. 8(b), which show a striking contrast to the trends for the Newtonian fluids; The jet speeds for the lowest viscosity ($\mu_0 = 0.09$ Pa.s) are in the range $V_j \approx 125 - 140$ m/s, similar to water, whilst the Newtonian equivalent ($\mu_0 = 0.084$ Pa.s) jet speeds are in the range $V_j \approx 100 - 120$ m/s, the effect of device configuration notwithstanding. As the CMC concentration increases, the low-shear viscosity also increases, and for $\mu_0 = 2.66$ the jet speeds are still $V_j \approx 110 - 120$ m/s, whereas the closest Newtonian equivalent (pure glycerol with $\mu = 1.31$ Pa.s) has a much reduced jet speed of 60–70 m/s. Even at the highest concentration of CMC with $\mu_0 = 343$ Pa.s, the jet speeds are only marginally diminished to $V_j \approx 95 - 120$ m/s. The fact that the device can sustain such a high jet velocity at these values of μ_0 can therefore only be explained by the high shear occurring near the orifice, rendering significantly reduced effective viscosities, μ_a, as per equation (1).

To quantitatively understand this effect, we can approximate the shear rates both at the plunger tip (upstream of the orifice) and at the orifice using the plunger and jet speeds, giving:

$$\dot{\gamma}_P \approx 2V_P/D_p, \quad \dot{\gamma}_j \approx 2V_j/D_j. \tag{3}$$

From these first-order approximations, we estimate the upstream shear rate to be $\dot{\gamma}_P \approx 50 - 70$ s^{-1}, whilst at the orifice $\dot{\gamma}_j \approx 1.2 \times 10^6 - 1.8 \times 10^6$ s^{-1}. The reduction in apparent viscosity based upon these shear rates can be quite dramatic, with $\mu_a \approx 0.06 - 4.5$ Pa.s in the plunger region and $\mu_a \approx 0.019 - 0.095$ Pa.s in the orifice region. This is best illustrated by re-plotting the non-Newtonian jet speeds in terms of μ_a along with the Newtonian counterparts, shown in Fig. 8(c) for the reduced volume configuration. As such, it is clear that the high shear rates experienced in the orifice region are a dominant factor for the performance of non-Newtonian fluids in injector devices.

With regards to hydrodynamic classifaction of the jet, only water jets are fully turbulent ($Re > 2 \times 10^4$), whilst 50% glycerol is in transitional flow ($Re \approx 3100$), and all other fluids are laminar ($Re < 1500$). Regardless of configuration, the approximate threshold for laminar flow at the orifice is $\mu^* \approx 10$ mPa.s. In particular, all of the non-Newtonian jets are laminar with $Re \lesssim 1000$, when taking the apparent viscosity (at the orifice) to calculate the Reynold number ($Re_j = \frac{\rho V_j D_j}{\mu_a}$). It is important to note that shear deformation at the orifice is not a consequence of molecular composition, rather a feature that may aid in achieving suitable jet speeds for solutions or suspensions of various active pharmaceuticals ingredients (APIs).

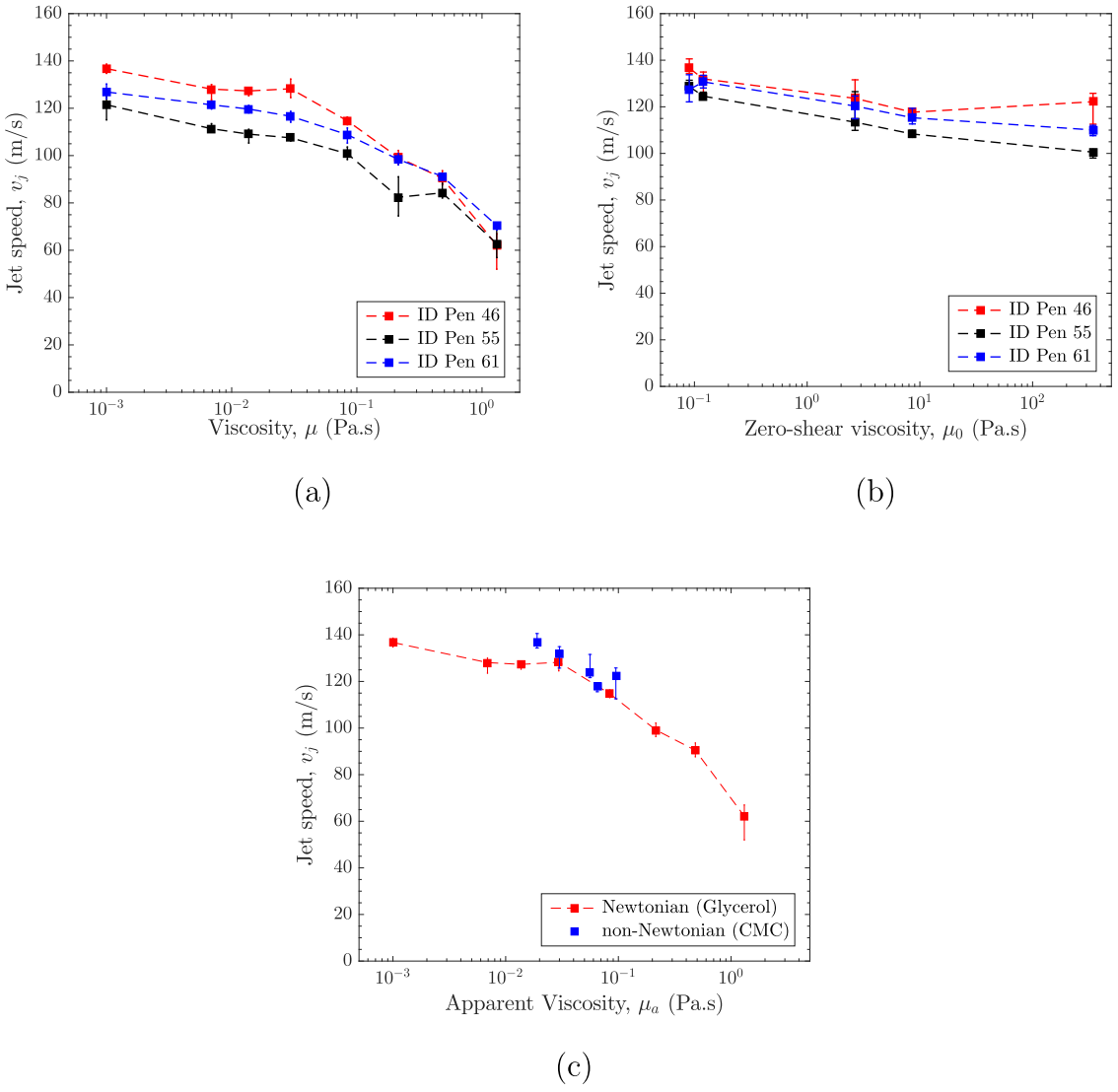

Fig. 8. Jet exit velocity calculated from equation (2) for (a) Glycerol solutions (b) CMC Solutions. In each plot the three data sets correspond the different ID Pen configurations (Blue = standard volume 100 μL and force 63 lbs/in, Red = reduced volume 50 μL, Black = reduced spring force 55 lbs/in). In (b), the x-axis is the zero shear viscosity, μ_0. (c) Comparison of glycerol and CMC jet speeds for Pen 46, plotted against apparent viscosity at the orifice. (For interpretation of the references to colour in this figure legend, the reader is referred to the Web version of this article.)

3.4. Peak impact force and pressure

In the true application of needle-free injectors, the flow that emerges from the orifice as a jet will ultimately impact and puncture the skin, and disperse in the underlying tissue. In this regard, the impact pressure or force of the jet is an important quantity, and previously, force measurements have been used as a means to derive jet speeds via momentum conservation [46] as $V_j = \sqrt{F/(\rho A)}$, where F is the force and $A = \pi D_o^2/4$ is the cross-sectional area of the orifice. As such, we measured the dynamic force of the jets using the load cell described in §2.4.

Fig. 9 provides an example force-time curve for water with the standard configuration, showing the salient features. The peak force, F^*, is registered within 1–2 ms, and corresponds to the pressure impulse in the displacement curves (see Fig. 7). Following this, we observe the short 'ringing' phase caused by compressibility of the plunger tip and the fluid before the steady plunger stage; the start and end of this stage are captured by the forces F_1 and F_2, respectively, as shown on the curve, and we quantify this stage with the mean steady force, $F_S = \frac{1}{2}(F_1 + F_2)$. In addition, we calculate the normalized steady force as the ratio of the mean steady force to the peak force, i.e. F_S/F^*. The reader should note that trends for the three device configurations seen in the jet speeds were also observed here, but for purposes of clarity these data are not shown, and the following discussion pertains to the standard configuration.

To start with, the peak force F^* is plotted as a function of viscosity in Fig. 10(a), for both Newtonian and non-Newtonian fluids. The overall trend for the Newtonian fluids largely mirrors that seen for the jet speeds; however, for the low-viscosity regime, the peak force does not decay in the same fashion as the speeds, whereby $F^* \approx 0.65 - 0.7$ N for $\mu \lesssim 30$ mPa.s, after which F^* decays gradually down to ≈ 0.26 N for pure glycerol ($\mu = 1310$ mPa.s). For the non-Newtonian fluids, we observe a sharper decrease in peak force across the full range of apparent viscosities, from $F^* \approx 0.76$ N to 0.42 N.

One important factor to keep in mind is that the peak force is associated with the pressure impulse when the injection is actuated and that a force of ≈ 0.5 N with an orifice diameter of 155 μm translates to a pressure of O(10) MPa, which is reported to be in the range needed to puncture porcine and human skin [32,50,51].

In Fig. 10(b), we present the mean steady-stream forces, F_S, averaged across the steady-stream phase, $F_1 \rightarrow F_2$, which exhibit

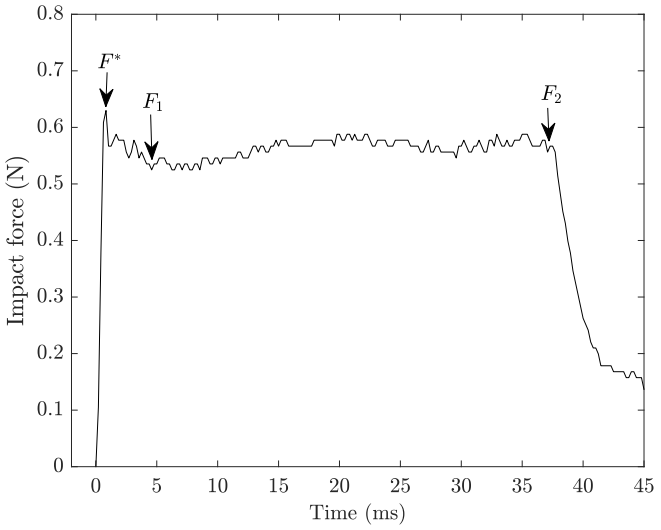

Fig. 9. Force-time curve for water jet impinging on the load cell with ID Pen 61 (standard configuration). The curve is annotated with definitions of Peak force, F^* and characteristic force points F_1 and F_2 along the force curve.

qualitatively similar trends to the peak force, but with a consistent reduction of between 0.1 and 0.2 N. We also observe more significant variation (larger error bars) in F_s for low-viscosity fluids ($\mu \leq 0.03$ Pa.s) compared to higher viscosities. This again could be partly due to deviations from a collimated jet stream causing discrepancies in measurements of F_1 and F_2, which would not be as prevalent in higher viscosity fluids.

Finally, in Fig. 10(c), we observe that the ratio of steady force to peak force is approximately 0.8 for the Newtonian fluids with $\mu \leq 0.215$ Pa.s, but 0.67 and 0.56 for $\mu = 0.482$ and 1.31 Pa.s, respectively. The ratio of steady-to-peak force provides an analogy to the 'two-stage' injection reported by Refs. [30,52], where the velocity in the initial and 'follow-through' stages (V_{jet} and V_{ft}) are more precisely controlled; In Ref. [52] the ratio of velocities was $V_{ft}/V_{jet} = 0.25$, which is significantly lower than the ratio of the forces herein.

As a concluding remark on the jet force, there is a discrepancy between the actual jet speeds from our high-resolution tracking compared to those derived from the force, assuming momentum conservation. To exemplify this, we consider the extreme cases of viscosity for water and glycerol as follows: For water, direct measurement of velocity from high-resolution tracking yields $V_j = 127$ m/s in the linear stage, whilst the force measurement in the linear stage, $F_s = 0.55$ N, leads to a value $V_j = \sqrt{F/(\rho A)} = 171$ m/s. This represents an error of 35%. In contrast, direct measurement for glycerol gave a velocity of 70.4 m/s, but the force measurement of 0.14 N yields a velocity of 76.7 m/s, giving an error of 9%. The fact that the error diminishes significantly for laminar jets compared to turbulent jets indicates that jet stream turbulence and dispersion (see Fig. 5 and refs [53,54]) must play some role. Another important factor is the effect of standoff between the orifice and the load cell; the impact pressure of water jets was shown to vary with standoff in a previous study [55]. Both jet stream collimation and standoff must therefore be carefully investigated in future studies of jet injection dynamics, along with high-resolution imaging and derivations of instantaneous jet speed.

3.5. Ex-vivo trials

For a practical demonstration of the effect of fluid properties, we performed ex-vivo injections into porcine tissue procured from the abdomen. Prior to injection, the outer layer of the skin was removed (as done in Ref. [34]) due to this layer being very stiff. The injection volume was 0.1 mL and the working fluids were water ($\mu = 0.001$ Pa.s), 80% glycerol ($\mu = 0.084$ Pa.s) and 0.5% CMC ($\mu_0 = 3.9$ Pa.s, $\mu_a \approx 0.056$ Pa.s). The tissue samples were placed directly under the orifice, thus yielding zero standoff distance. All fluids were augmented with blue dye to aid visualization, and the injection sites were section medially with a sharp blade to measure the injection depth and lateral distribution, as shown in Fig. 11. The jet path in the upper fat layer can clearly be seen, followed by a more diffuse pattern in the tissue below. The injection in this realization appears to have stopped at the boundary of the second fat layer, which was a consistent observation.

To quantify the injections, we first calculate the injection efficiency, $E_{\%}$, which represents the ratio of the liquid volume delivered into the porcine tissue, V_{inj}, from the total volume of the liquid ejected from the orifice, $V_{ej} = 0.1$ mL, as per equation (4):

$$E_{\%} = 100 \times \frac{V_{inj}}{V_{ej}} \tag{4}$$

For the three fluids investigated here, injection efficiency is always above 70% and generally increases in order as water < 80% glycerol < 0.5% CMC as shown in Fig. 12. That is, the median injection efficiency increases from water to 80% glycerol to 0.5% CMC, but we also observe decreasing variability showing that, with regards to injection efficiency, 0.5% CMC is superior. From a statistical perspective, single-factor ANOVA indicates that the effect of fluid properties is moderately significant ($P = 0.061$). An injection efficiency less than 100% indicates that some fluid is rejected and pooled on top of the tissue. Clearly, characteristics of the tissue, which is a poro-elastic heterogeneous matrix, play an important role in the injection dynamics. However, since all injections herein were performed into the same sample source, the variability in injection efficiency indicates that the fluid properties, and hence jet characteristics (speed and collimation) are the key factors. The improved performance of the 0.5% CMC may be a manifestation of a preferential balance between jet speed and collimation for this fluid. Either way, the fact that the non-Newtonian fluid improves performance may prove to be an asset for inherently complex drug formulations, such as DNA vaccines.

A secondary quantification of the injection can be garnered from the dispersion patterns, characterized by both the injection depth (H) and width (W), and aspect ratio (W/H). Fig. 13(a) plots the total ranges of both widths and heights for all three liquids. Here, we observe that all of the injections are centered around injection depths of $H \approx 1 - 1.2$ cm and widths of $W \approx 0.9 - 1.1$ cm. Again from a statistical standpoint, the fluid properties has a moderately significant effect on the injection depth ($P = 0.071$), but no effect on the width ($P = 0.39$). Combining the two principal dimensions, we calculate the aspect ratio as W/H, presented in Fig. 13(b), which shows that the majority of injections occur in the regime $W/H \leq 1$. That is to say the injection dispersion patterns are logitudinal, which is evident from the medial sections such as that shown in Fig. 11. These dispersion patterns are qualitatively similar to those of [52] with streamline jets, whereas their injections with a dispersed jet resulted in shallower bolus formations in the upper fat layer only. Future studies could therefore investigate the compound effect of both fluid viscosity and jet dispersion, promoted by irregular orifice shapes.

4. Conclusions

We have conducted a broad study of the effect of fluid properties in spring-actuated jet injection. The primary quantitative measurements were jet speed, impact force, and injection efficiency. For jet speed, which was derived by direct displacement using high-speed video, we found that the speed diminishes from $V_{jet} \approx 120 - 140$ m/s for water ($\mu = 0.001$ Pa.s) down to $V_{jet} \approx 60 - 70$ m/s for glycerol ($\mu = 1.3$ Pa.s). However, for the non-Newtonian fluids, with a wide range of low-shear viscosities ($\mu_0 \approx 10^{-1} - 4 \times 10^2$), the jet speeds were in the range $V_{jet} \approx 120 - 140$ m/s, and did not exhibit a strong dependence on

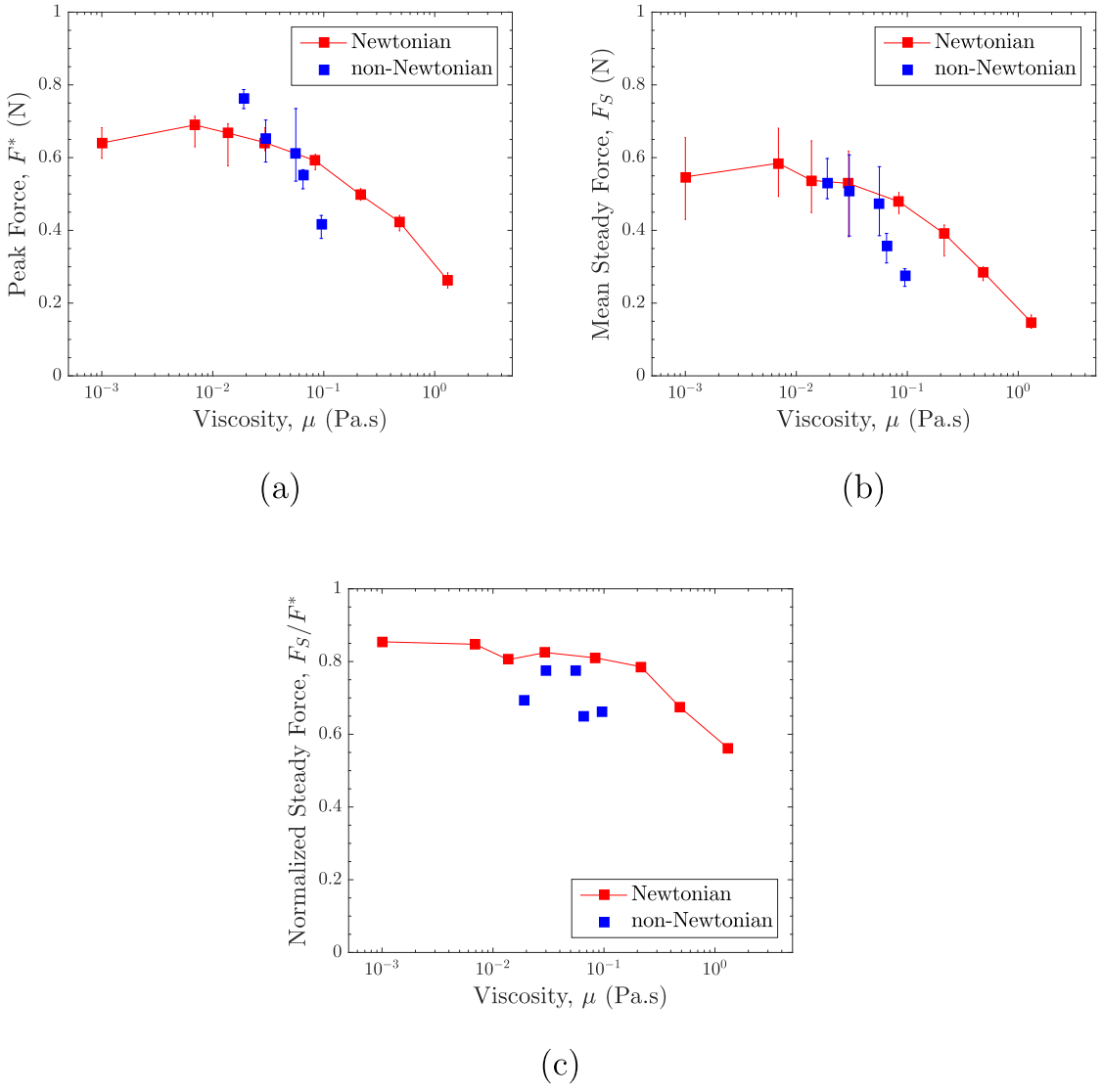

Fig. 10. (a) Peak impact force, and (b) Mean steady force for different liquids, plotted against viscosity. For non-Newtonian fluids, the viscosity is the apparent viscosity based upon the average shear rate at the orifice (equation (3)). (c) Normalized steady force.

Fig. 11. Photograph of the medial section of an injection of 0.1 mL of 80% glycerol into porcine abdomen tissue. The scale bar is 1 cm long, indicating injection depth and width are $H \approx 1$ cm and $W \approx 0.77$ cm in this realization.

concentration of the polymer. This could be partly reasoned by the high-shear near the orifice, $\dot{\gamma} \sim \mathcal{O}(10^6)$, rendering effective viscosities for all solutions in range $\mu_a = 10^{-2} - 10^{-1}$. This indicates that the high-shear region in the orifice is a dominant factor in the hydrodynamics and can render jet speeds high enough for skin puncture and efficient jet injection, even for high-concentration or high molecular weight solutions.

In terms of impact force, we found that the peak impact forces ($t < 2$

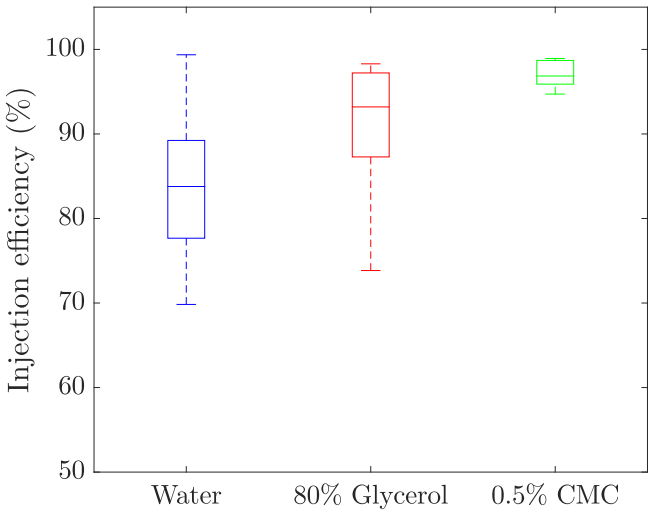

Fig. 12. Injection efficiency into porcine tissue for different liquids.

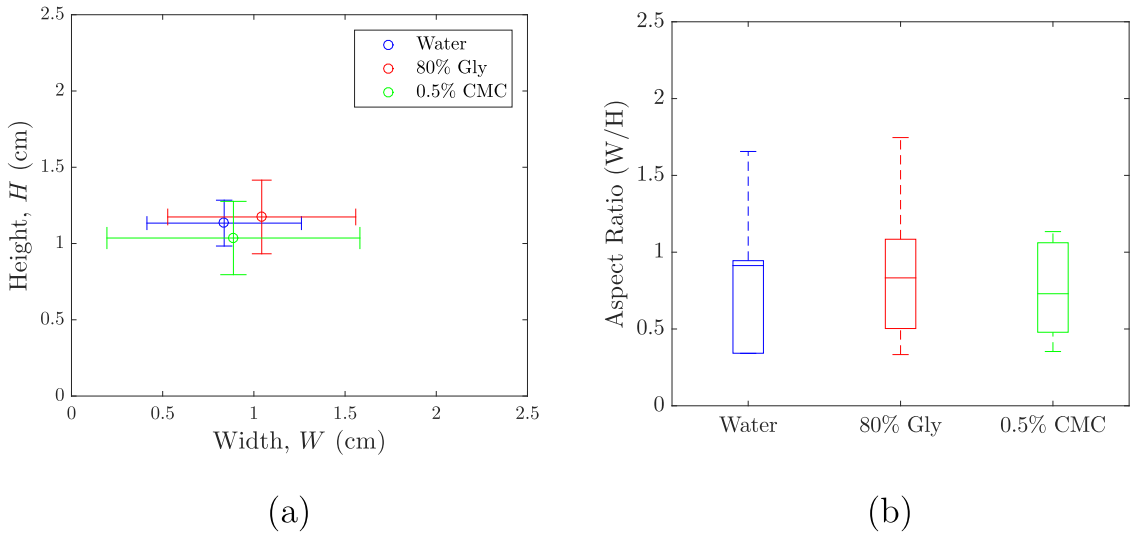

Fig. 13. Bleb dimensions (a) aspect ratio of blebs for different liquids, (b) width vs height of blebs for different liquids.

ms) were consistently in the range 0.25–0.7 N, and the mean force associated with the steady stream were slightly lower by around 0.1 N. The values of force did not correspond to the force based upon momentum at the orifice $\sim \rho A V_j^2$, especially for the low-viscosity fluids, which we hypothesize is due to an interplay between jet dispersion and axial velocity profile. This highlights the importance of using direct velocity measurements to characterize jet injector systems, rather than relying on impact force alone.

Ex-vivo injections into porcine tissue which contained strips of both muscle and subcutaneous fat indicated that fluid properties were significant in determining injection efficiency and depth, with the shear-thinning fluid (0.5%$_{w/w}$ CMC) providing the most consistent injection with $E_{\%} \geq 95\%$.

Overall, our results are especially promising for delivery of nucleic acids (e.g. DNA-based vaccines and therapeutics), which are shear-thinning and may need high concentrations to achieve immune response.

Acknowledgments

This work was financially supported by Inovio Pharmaceuticals and National Science Foundation via award number NSF-CBET-1749382.

References

[1] Y. Nir, A. Paz, E. Sabo, J. Potasman, Fear of injection in young adults: prevalence and associations, Am. J. Trop. Med. Hyg. 68 (2004) 341–344.
[2] C.M. McMurty, M. Noel, A. Taddio, M.M. Antony, G.J.G. Asmundson, R.P. Riddel, C.T. Chambers, V. Shah, Intervention for individuals with high levels of needle fear: systematic review of randomized controlled trials and quasi-randomized controlled trials *Clinical*, J. Pain 31 (2015) S109.
[3] M. Kakizaki, N. Ikeda, M. Ali, B. Enkhtuya, M. Tsolmon, K. Shibuya, C. Kuroiwa, Needlestick and sharps injuries among healthcare worker at public tertiary hospitals in an urban community in Mongolia, BMC Res. Notes 4 (1) (2011) 184.
[4] A. Kane, J. Lloyd, M. Zaffran, L. Simonsen, M. Kane, Transmission of hepatitis B, hepatitis C and human immunodeficiency viruses through unsafe injections in the developing world: model-based estimates, Bull. WHO 77 (1999) 801–807.
[5] The World Health Report, Reducing Risks, Promoting Healthy Life, (2002).
[6] A. Mannocci, G. De Carli, V. Di Bari, R. Saulle, B. Unim, N. Nicolotti, L. Carbonari, V. Puro, G. La Torre, How much do Needlestick injuries cost? A systematic review of the economic evaluations of needlestick and sharps injuries among healthcare personnel, Infect. Control Hosp. Epidemiol. 37 (2016) 635–646.
[7] J. Jagger, E.H. Hunt, R.D. Pearson, Estimated cost of needlestick injuries for six major needled devices, Infect. Control Hosp. Epidemiol. 11 (1990) 584–588.
[8] Proceedings of the Annual Meeting of the Safe Injection Global Network, Dubai, (2010).
[9] Assessment Report of the Global Vaccine Action Plan, (2014).
[10] S. Mitragotri, Immunization without needles Nat. Rev. Immunol. 5 (3) (2005) 905–916.
[11] S. Mitragotri, Current status and future prospects of needle-free liquid jet injectors, Nat. Rev. Drug Discov. 5 (2006) 543–548.
[12] R.A. Hingson, J.G. Hughes, Clinical studies with jet injection: a new method of drug administration, Curr. Res. Anesth. Analg. 26 (1947) 221–230.
[13] N. Inoue, H. Todo, D. Iidaka, Y. Tokudome, F. Hashimoto, t. Kishino, K. Sugibayashi, Possibility and effectiveness of drug delivery to skin by needle-free injector, Int. J. Pharm. 391 (2010) 65–72.
[14] K. Benedek, E. Walker, L.A. Doshier, R. Stout, Studies on the use of needle-free injection device on proteins, J. Chromot. A 1079 (2005) 397–407.
[15] A. Bavdekar, J. Oswal, P.V. Ramanan, et al., Immunogenicity and safety of measles-mumps-rubella vaccine delivered by disposable-syringe jet injector in India: a randomized, parallel group, non-inferiority trial, Vaccine 36 (2018) 1220–1226.
[16] M.T. Yousafzai, A.F. Saleem, O. Mach, A. Baig, R.W. Sutter, A.K.M. Zaidi, Feasibility of Conducting Intradermal Vaccination Campaign with Inactivated Poliovirus Using Tropis Intradermal Needlefree Injection System, Karachi, Pakistan, Heliyon 3 (2017) e00395.
[17] S. Resik, A. Tejeda, O. Mach, C. Sein, N. Molodecky, C. Jarrahian, L. Saganic, D. Zehrung, M. Fonesca, M. Diaz, N. Alemany, G. Garcia, L.H. Hung, Y. Martinez, R.W. Sutter, Needle-free jet injector intradermal delivery of fractional dose inactivated poliovirus vaccine: association between injection quality and immunogenicity, Vaccine 33 (2015) 5873–5877.
[18] D. Soonawala, P. Verdijk, Wijmenga-Monsuur, C.J. Boog, P. Koedam, L.G. Visser, N.Y. Rots, Intradermal fractional booster of inactivated poliomyelitis vaccine with a jet injector in healthy adults, Vaccine 31 (2013) 3688–3694.
[19] J.K. Simon, C. Michaela, M.F. Pasetti, et al., Safety, tolerability, and immunogenicity of inactivated trivalent seasonal influenza vaccine administered with a needle-free disposable syringe jet injector, Vaccine 29 (2011) 9544–9550.
[20] A.J. Mohammed, S. Al-Awaidy, S. Bawikar, et al., Fractional doses of inactivated poliovirus vaccine in Oman, N.E. J. Med. 365 (25) (2010) 2351–2359.
[21] X. Li, B. Ruddy, A. Taberner, Characterization of needle-assisted jet injections, J. Control. Release 243 (2016) 195–203.
[22] T.M. Grant, K.D. Stockwell, J.B. Morrison, D.D. Mann, Effect of injection pressure and fluid volume and density on the jet dispersion pattern of needle-free injection devices, Biosyst. Eng. 138 (2015) 59–64.
[23] J.C. Stachowiak, T.H. Li, Anubhav Arora, S. Mitragotri, D.A. Fletcher, Dynamic control of needle-free jet injection, J. Control. Release 135 (2009) 104–112.
[24] A. Arora, M.R. Prausnitz, S. Mitragotri, Micro-scale devices for transdermal drug delivery, Int. J. Pharm. 364 (2008) 227–236.
[25] J.C. Stachowiak, M.G. von Muhlen, T.H. Li, L. Jalilian, S.H. Parekh, D.A. Fletcher, Piezoelectric control of needle-free transdermal drug delivery, J. Control. Release 124 (2007) 88–97.
[26] O.A. Shergold, N.A. Fleck, T.S. King, The penetration of a soft solid by a liquid jet, with application to the administration of a needle-free injection, J. Biomech. 39 (2006) 2593–2602.
[27] J. Schramm-Baxter, J. Katrencik, S. Mitragotri, Jet injection into polyacrylamide gels: investigation of jet injection mechanics, J. Biomech. 37 (2004) 1181–1188.
[28] J.W. McKeage, B.P. Ruddy, P.M.F. Nielsen, A.J. Taberner, The effect of jet speed on large volume jet injection, J. Control. Release 280 (2018) 51–57.
[29] J.W. McKeage, B.P. Ruddy, P.M.F. Nielsen, A.J. Taberner, Power-efficient controlled jet injection using a compund ampoule, J. Control. Release 291 (2018) 127–134.
[30] J.W. McKeage, K.A. Brennan, G. Park, C.A. Hogan, I.W. Hunter, B.P. Ruddy, P.M.F. Nielsen, A.J. Taberner, High-speed X-ray analysis of liquid delivery during jet injection, Trans. IEEE (2017) 296–299.
[31] A. Taberner, N.C. Hogan, I.W. Hunter, Needle-free injection using real-time controlled linear Lorentz-force actuators, Med. Eng. Phys. 34 (2012) 1228–1235.
[32] J. Baxter, S. Mitragotri, Jet-induced skin puncture and its impact on needle-free jet

injections: experimental studies and a predictive model, J. Control. Release 106 (2005) 361–373.
[33] J. Schramm-Baxter, S. Mitragotri, Needle-free jet injections: dependence of jet penetration and dispersion in the skin on jet power, J. Control. Release 97 (2004) 527–535.
[34] J. Schramm, S. Mitragotri, Transdermal drug delivery by jet injectors: energetics of jet formation and penetration, Pharm. Res. 19 (2002) 1673–1679.
[35] A. Arora, I. Hakim, Rathnasingham, R. Srinivasan, D.A. Fletcher, S. Mitragotri, Needle-free delivery of macromolecules across the skin by nanoliter-volume pulsed microjets, Proc. Natl. Acad. Sci. 104 (2007) 4255–4260.
[36] A. Kiyama, N. Endo, S. Kawamoto, C. Katsuta, k. Oida, A. Tanaka, Y. Tagawa, Visualization of penetration of a high-speed focused microjet into gel and animal skin, J. Vis. (2019), https://doi.org/10.1007/s12650-019-00547-8.
[37] P. Delrot, S.P. Hauser, J. Krizek, C. Moser, Depth-controlled laser-induced jet injection for direct three-dimensional liquid delivery, Appl. Phys. A 124 (2018) 615.
[38] C. Berrospe-Rodriguez, C.W. Visser, S. Schlautmann, D.F. Rivas, R. Ramos-Garcia, Toward jet injection by continuous wave laser cavitation, J. Biomed. Opt. 22 (2017) 105003.
[39] Y. Tagawa, N. Oudalov, A. El Ghalbzouri, C. Sun, D. Lohse, Needle-free injection into skin and soft matter with highly focused microjets, Lab Chip 13 (2013) 1357.
[40] H. Miyazaki, S. Atobe, T. Suzuki, H. Iga, K. Terai, Development of a pyro-drive jet injector with controllable jet pressure J. Pharm. Sci. https://doi.org/10.1016/j.xphs.2019.02.021.
[41] D.S. Tomar, S. Kumar, S.K. Singh, S. Goswami, L. Li, Molecular basis of high viscosity in concentrated antibody solutions: strategies for high concentration drug product development, mAbs 8 (2) (2016) 216–228.
[42] F. Cilurzo, F. Selmin, P. Minghetti, M. Adami, E. Bertoni, S. Lauria, L. Montanari, Inject. Eval.: An Open Issue Pharm. Sci. Tech. 12 (2011) 604–609.
[43] M.A. Liu, DNA vaccines: a review, J. Intern. Med. 253 (2003) 402–410.
[44] J. Rice, C.H. Ottensmeier, F. Stevenson, DNA vaccines: precision tools for activating effective immunity against cancer, Nat. Rev. Cancer 8 (2008) 108–120.
[45] S.S.A.A. Hasson, J.K.Z. Al-Busaidi, T.A. Sallam, The past, current and future trends in DNA vaccine immunizations, Asian Pacific J. Top. Biomed. 5 (2015) 344–353.
[46] R.M.J. Williams, B.P. Ruddy, N.C. Hogan, I.W. Hunter, P.M.F. Nielsen, A.J. Taberner, Analysis of moving-coil actuator jet injectors for viscous fluids, IEEE Trans. Biomed. Eng. 63 (6) (2016) 1099–1106.
[47] R.M.J. Williams, J.W. McKeage, B.P. Ruddy, P.M.F. Nielsen, A.J. Taberner, Viscous heating assists jet formation during needle-free jet injection of viscous drugs, IEEE Trans. Biomed. Eng. (2016), https://doi.org/10.1109/TBME.2019.2906356.
[48] A. Benchabane, K. Bekkour, Rheological properties of carboxymethyl cellulose (CMC) solutions, Colloid Polym. Sci. 286 (10) (2008) 1173.
[49] M.T. Ghannam, M.N. Esmail, Rheological properties of carboxymethyl cellulose, J. Appl. Polym. Sci. 64 (2) (1997) 289–301.
[50] J. Ankersen, A.E. Birkbeck, R.D. Thomson, P. Vanezis, Puncture resistance and tensile strength of skin simulants, Proc. Inst. Mech. Eng. H J. Eng. Med. 211 (6) (1999) 493–501.
[51] L.H. Jansen, P.B. Rottier, Some mechanical properties of human andominal skin measured on excised strips, Dermatologica 117 (1958) 65–83.
[52] G. Park, A. Modak, N.C. Hogan, I.A. Hunter, The effect of jet shape on jet injection, Trans. IEEE (2015) 7350–7353.
[53] S.P. Lin, R.D. Reitz, Drop and spray formation from a liquid jet, Annu. Rev. Fluid Mech. 30 (1998) 85–105.
[54] M.J. McCarthy, N.A. Molloy, Review of stability of liquid jets and the influence of nozzle design, Chem. Eng. J. 7 (1) (1974) 1.
[55] W. Sittiwong, W. Seehanam, K. Pianthong, A. Mutthujak, Effect of stand-off distance on impact pressure of high-speed water jets, AIP Conf. Proc. 1225 (2010) 864–873.